Journal of Microscopy, Vol. 194, Pt 1, April 1999, pp. 58–70.
Received 20 April 1998; accepted 15 October 1998

Energy-filtered transmission electron microscopy of multilayers in semiconductors

C. P. LIU, C. B. BOOTHROYD & C. J. HUMPHREYS
Department of Materials Science and Metallurgy, University of Cambridge, Pembroke Street, Cambridge CB2 3QZ, U.K.

Key words. EFTEM, ESI, InAsP, multilayers, quantitative analysis, semiconductors, TiAlN.

Summary

Quantitative analysis of novel semiconductors with wide or ultrathin multilayers of atomic dimensions is very important in order to control electronic and optical properties, but rather difficult due to the limited resolution in most techniques. In this paper we attempt to assess how effectively the total As dopant concentration in ultrathin As doped layers in InP and the Ti atomic fraction in a $Ti_xAl_{1-x}N$ multilayer can be analysed quantitatively using energy-filtered imaging. These two materials have characteristic edges located at widely different energy losses, with the L edge of As being above 1000 eV, while that of Ti is around 450 eV. We have quantified the As concentration using the three-window technique and theoretical cross-sections and we find that the resolution limit is dominated by the signal-to-noise ratio in this delta-doped specimen. However, the accuracy of the Ti atomic fraction in $Ti_xAl_{1-x}N$ can be as good as 10 at% for specimens of uniform thickness made by focused ion beam milling. We will compare our results with measurements of the composition made using Fresnel contrast, high resolution imaging and high angle annular dark field techniques.

Introduction

There are many examples of semiconductor structures where the interfacial compositional profile needs to be determined on an atomic scale. For example, for $Ti_xAl_{1-x}N$ multilayers acting as a potential diffusion barrier in silicon-based semiconductor devices, we require an accurate knowledge of the layer composition in order to investigate the interfacial reactions between each layer. In addition, $InAs_xP_{1-x}$ doping layers a few monolayers or less wide in InP semiconductors that emit laser light in the 1·0–2·0 μm wavelength range and perform better than lattice-matched semiconductor systems also require very accurate compositional profiles of As in such layers in order to control the electrical and optical properties of such devices. However, very few techniques can be used to characterize them to monolayer accuracy.

The use of electron spectroscopic imaging (ESI) in an energy-filtered transmission electron microscope (EFTEM) has attracted much attention not only because of the capability of quantitative analysis but because of the ability to directly observe the elemental distribution in two dimensions (e.g. Wang, 1996). However, for quantitative composition analysis from energy-filtered images, some problems are still present. Firstly, the specimen must be thin since it is usually assumed that the quantitative signal is dominated by single scattering. Consequently, for elemental analysis with edges below 1000 eV, plural scattering can be ignored only when the ratio of the specimen thickness to the total inelastic mean free path, $t/\lambda < 0{\cdot}5$ (Crozier, 1995), while for edges above 1000 eV, quantitative analysis can be extended to thicker regions up to $t/\lambda = 2$ (Egerton *et al.*, 1991). Secondly, background signal on an energy-loss spectrum is difficult to be subtracted very accurately and the choice of the methods of background fitting is dependent on the specific edge of elements (Crozier, 1995). Thirdly, diffraction effects often dominate the contrast of ESI images at lower energy losses and the poor signal-to-noise ratio for the edges at energy losses above 1000 eV is often found to limit the application of quantitative analysis on materials of this kind (Jager & Mayer, 1995). Nonetheless, in principle quantitative data can be extracted from the background-subtracted images using the integration method (Egerton, 1997).

In this paper, two types of specimen representing characteristic edges falling in the low and high energy loss regime will be examined. The first specimen contains six wide $Ti_xAl_{1-x}N$ layers of unknown atomic ratio sandwiched between pure TiN and AlN layers, which served as calibration layers, deposited on Si allowing the atomic ratio

Correspondence to: C. B. Boothroyd. Tel: +44 (0)1223 334564; fax: +44 (0)1223 334567; e-mail: cbb4@cam.ac.uk

© 1999 The Royal Microscopical Society

to be studied for edges in the low energy region (the L edges of Ti and N are around 400 eV), while the second specimen contains six $In_xAs_{1-x}P$ delta-doped layers in InP and the interest here is the investigation of the absolute total dopant concentrations for an edge in the high energy region (the L edge of As is around 1350 eV). We will discuss how effectively this technique can be used for quantitative analysis by comparing data extracted from this technique with those obtained from other techniques including electron energy loss spectroscopy (EELS), the Fresnel method, high resolution imaging and high angle annular dark field (HAADF). We will also show how specimen preparation by focused ion beam (FIB) milling and cleaving makes quantitative analysis more feasible.

The determination of optimum experimental parameters

One problem in taking energy-filtered images is the choice of the experimental conditions such as aperture size, beam convergence, position of energy window, size of slit and exposure time for optimum resolution. Therefore, the factors limiting the resolution should be fully understood in order to acquire experimental images with the highest spatial resolution and accuracy, especially for highly demanding materials such as the delta-doped semiconductors studied here. Krivanek *et al.* (1995) have summarized eight basic factors which are: (1) delocalization of inelastic scattering, (2) chromatic aberration of the objective lens, (3) the diffraction limit due to the objective aperture, (4) spherical aberration due to the objective lens, (5) noise, (6) radiation damage, (7) instrumental instability and (8) resolution lost due to the electron image detector that affects the resolution of EFTEM inner-shell loss images. They recommended a formula to account for each factor (1)–(4) in calculations because only the first four terms depend on the instrument and have a fundamental effect on the resolution. Using these formulae, the spatial resolution for the JEOL 4000FX microscope ($C_s = 2{\cdot}0$ mm, $C_c = 1{\cdot}4$ mm) used for this study can now be calculated by summing up all of the contributions. The energy losses of the In(M45), As(L) and P(L) edges are 450, 1350 and 150 eV, respectively. Calculations of the spatial resolution for the Ti and N edges will give approximately the same results as for the In edge since they are all close to each other in energy. Figure 1 shows the calculated spatial resolution for: (a) In, (b) As, (c) P edges with a slit width w of 20 eV as a function of the semi-angle of the objective aperture, θ_0, while Fig. 2 shows the dependence of the resolution on the slit width, w, for In, As and P, respectively. It can be seen that the optimum resolution will move toward the smaller θ_0 when the slit width is increased, because there is a greater contribution from chromatic aberration from a wider slit resulting in the resolution worsening with larger θ_0. The trend of the change in spatial resolution with slit width is the same regardless of the edge

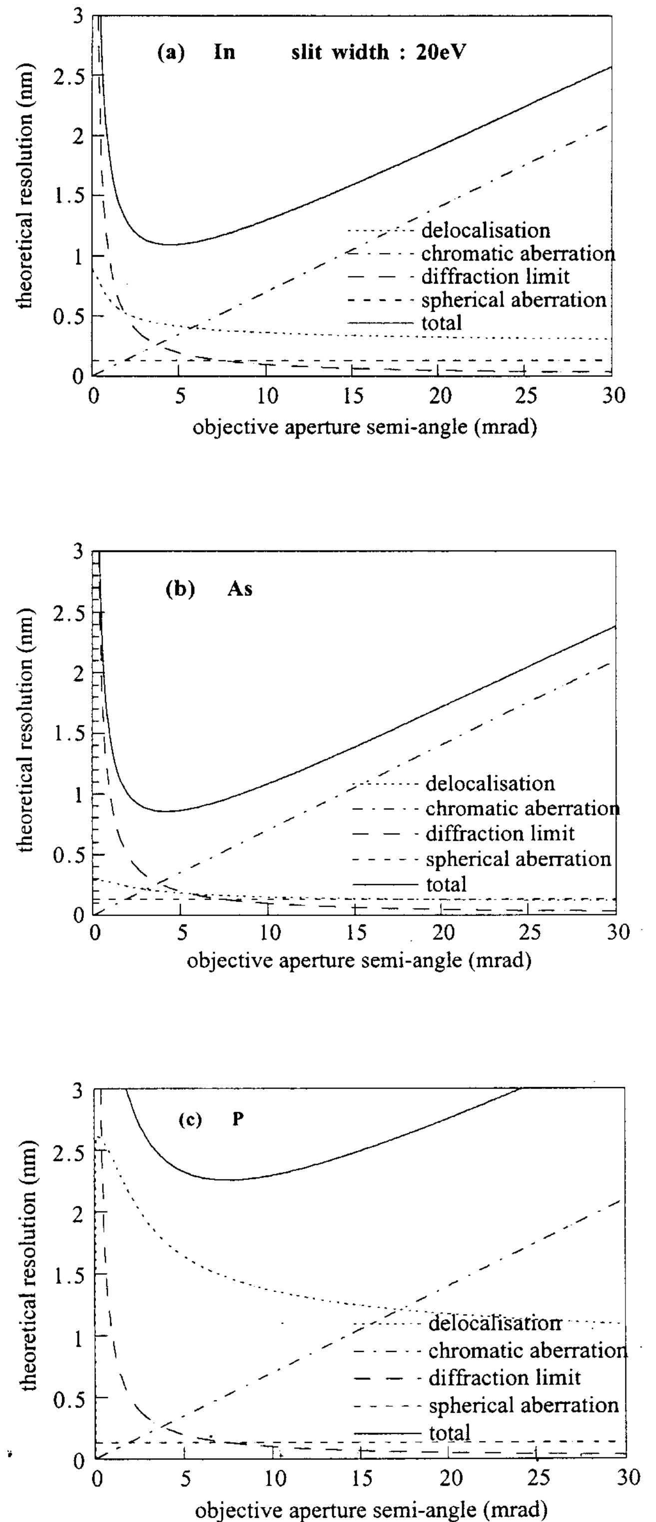

Fig. 1. Theoretical resolution for energy filtered images taken on a JEOL 4000FX operated at 400 keV as a function of the semiangle of objective aperture, θ_0, for energy loss maps at the (a) In, (b) As, (c) P edges and a slit width, w, of 20 eV.

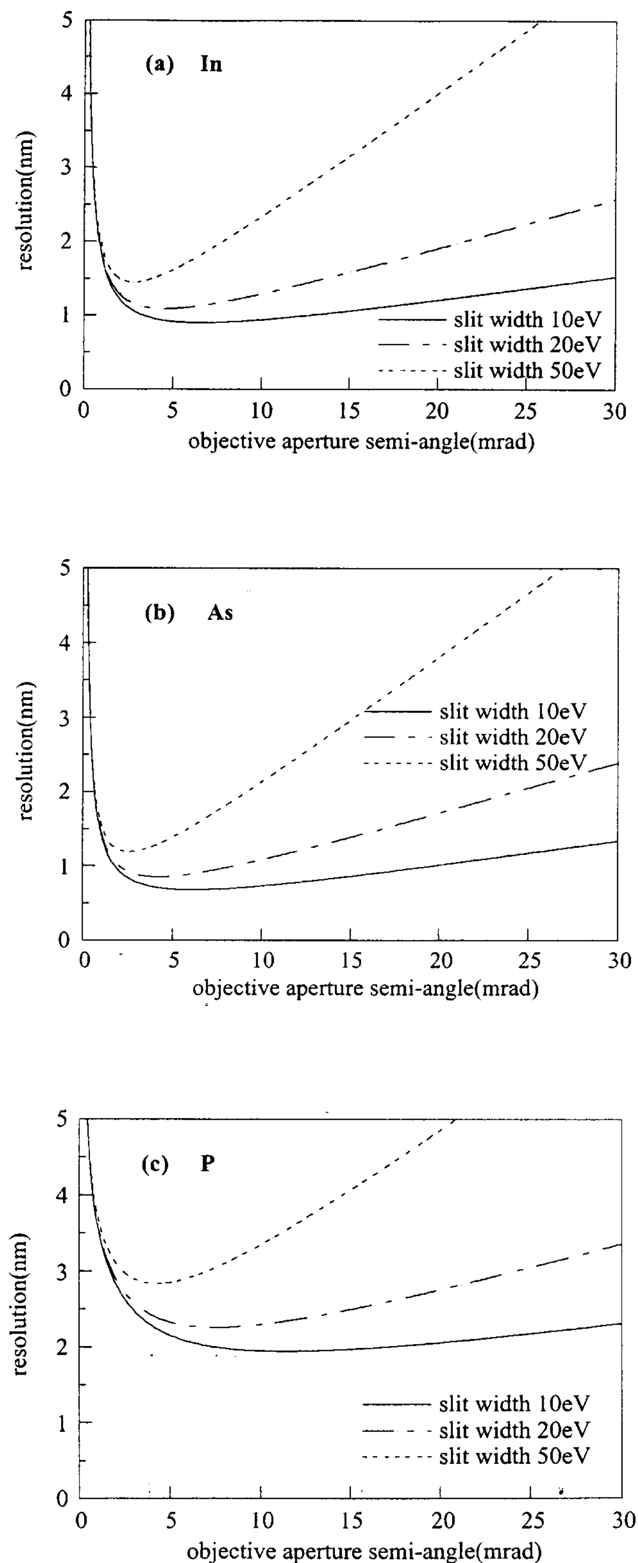

Fig. 2. The dependence of the resolution on the slit width, *w*, for the (a) In, (b) As and (c) P edges.

of energy loss. The dependence of the optimum resolution attainable for these three elements representing three different ranges of energy loss is not linear, and is 2·3 nm for P and around 1 nm for In and As.

Instead of expressing the resolution by summing up individual factors in the form of a disc of confusion, Egerton & Crozier (1997) characterized each lens aberration in terms of 50% of a point spread function (PSF), essentially the intensity distribution (in the image) which would result from a point object scattering electrons with a specified angular and energy distribution. They derived a PSF for the lens aberrations, C_c and C_s, using geometrical optics and found the shape of the PSF was influenced by the angular distribution of the inelastic electrons. In their treatment, the chromatic aberration has a smaller influence than the delocalization term on determining the resolution. Accordingly, the resolution determined by Egerton and Crozier's approach is better than that determined by Krivanek *et al*'s approach by a factor of 3–4. Nevertheless, the dependence of the resolution on the objective aperture size derived from Egerton and Crozier's approach is similar to Figs 1 and 2.

Jager & Mayer (1995) have explored the detection and resolution limits by acquiring Si elemental maps using the Si L edge from Si–Ge superlattices. They estimated that the detection limit is as good as 1–2 at% for the good signal to noise ratio of this relatively low energy loss edge and that the spatial resolution is about 1 nm. However, both limits depend on the signal-to-noise ratio and they also pointed out that it is very difficult to obtain a useful elemental map for Ge (L edge at 1200 eV) due to the poor signal-to-noise ratio.

One of the potential problems associated with energy filtered imaging is that the number of electrons collected for high energy losses within a reasonable exposure time might be too few to give sufficient signal so that the resolution is controlled by the signal-to-noise ratio. Berger & Kohl (1993) have derived a formula for resolution based on the signal-to-noise ratio which uses the criterion that this ratio should be no less than 5. A simpler formula is given by Kohl & Berger (1995) and we have applied this to As, since its L edge is above 1000 eV and thus a low signal is expected. For the calculation of signal-to-noise ratio, the acquisition time was taken to be 20 s and we have calculated theoretical cross sections for As which yields signal and for In, P which generate the background under the As edge. Accordingly, the dependence of the signal-to-noise ratio on the current density is shown in Fig. 3 for collection angles of 2·3 and 9·3 mrad. The signal-to-noise ratio rises with the slit width as well as with the collection angle as more electrons are allowed to contribute to the images. Figures 1 to 3 provide useful theoretical guidance for choosing the optimum experimental parameters. If an exposure time of 20 s can provide enough signal, then an objective aperture of 2·3 mrad and a slit width of 20 eV will give the best resolution.

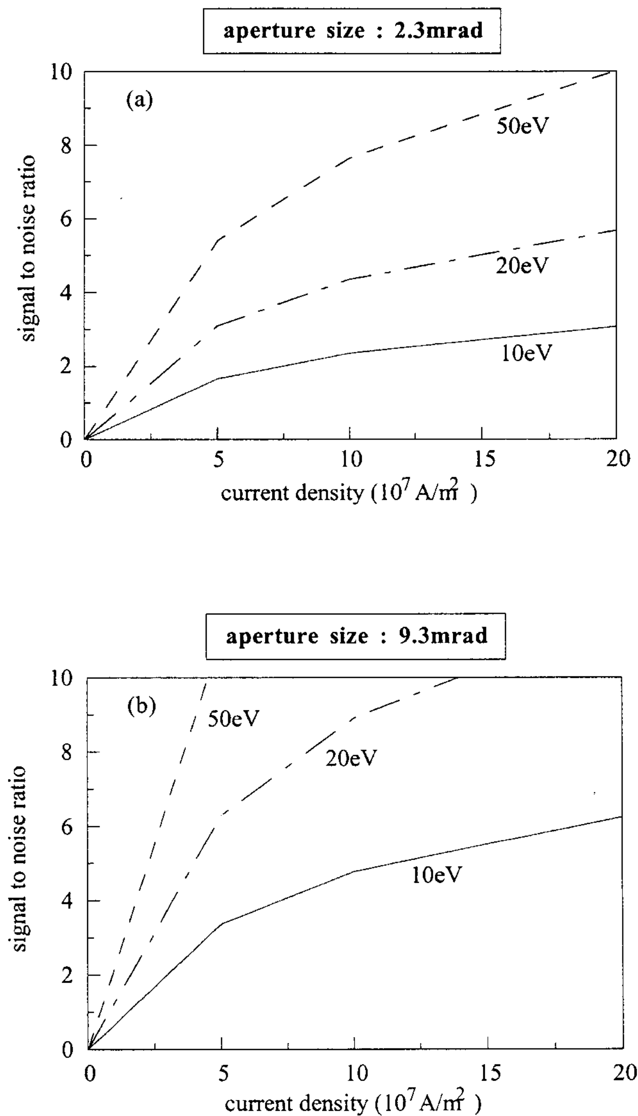

Fig. 3. The dependence of the signal-to-noise ratio on the current density for collection angles of (a) 2·3 mrad and (b) 9·3 mrad.

Experimental

The experiments were performed using a JEOL 4000FX electron microscope with a LaB_6 filament operating at 400 keV equipped with a postcolumn Gatan imaging filter (GIF). The experimental conditions have been described in an earlier paper (Liu *et al.*, 1998), but it is useful to repeat the major details here. The spectra and images were recorded with a 1 k × 1 k slow scan CCD camera binned by a factor of 2.

Two types of specimen are examined here. The $Ti_xAl_{1-x}N$ sample was reactively deposited onto a Si substrate by magnetron sputtering at room temperature, first pure TiN followed by six $Ti_xAl_{1-x}N$ layers with different sputtering times followed by pure AlN, with each layer separated by Al, forming a sandwich structure of the form TiN/Al/$Ti_xAl_{1-x}N$/Al/AlN/Al with a thickness of around 40 nm for the $Ti_xAl_{1-x}N$ layers and 20 nm for the Al layers. The $In_xAs_{1-x}P$ was grown by metal organic molecular beam epitaxy, constituting a sequence of InP layers on (001) InP, between each of which the growth was interrupted in the presence of As_2 for periods of 1, 2, 4, 8, 16 and 32 s at 500°C. The As doped layers were separated by 20 nm of InP, and their thickness was only a few monolayers. A TEM specimen of the $Ti_xAl_{1-x}N$ material was prepared using FIB milling, resulting in a specimen where the thickness is almost identical everywhere, making quantitative analysis easier, while the specimen of $In_xAs_{1-x}P$ was prepared in the form of 90° wedges by cleaving on {110} planes, making the measurement of sample thickness easier and more accurate. Since the optimum focus for an energy filtered image differs significantly from that for an elastic bright-field image, the energy filtered images were always focused at an energy loss of up to 500 eV. To obtain high intensities and resolution in the final image, the electron beam was always focused onto the region of interest on the specimen after the energy shift had been applied to allow for the change in condenser focus as the microscope voltage is changed. Both specimens were tilted so that the layers were edge-on, while the $In_xAs_{1-x}P$ sample was further tilted far off any major zone axis to avoid diffraction effects. Care was taken to ensure that knock-on damage was minimized when operating with 400 keV electrons by always aligning the microscope away from areas of interest.

The image processing procedure followed the standard procedure for the three-window, two-window and jump ratio methods. The critical step influencing the results was found to be the correction of specimen drift between images. Subsequently, all of the final images were divided by the 0 eV filtered image acquired with a slit width of 20 eV to reduce diffraction effects and extract quantitative data.

Results and discussion

$Ti_xAl_{1-x}N$ – edges below 1000 eV energy loss

The object for this specimen was to obtain the atomic fractions of Ti and Al for each $Ti_xAl_{1-x}N$ layer using the AlN and TiN layers for calibration. Figure 4 shows unfiltered and filtered bright field images of the $Ti_xAl_{1-x}N$ sample, and a thickness/total inelastic mean free path (t/λ) map calculated by taking the ratio of the unfiltered image to the zero-loss image. All of the layers are polycrystalline and exhibit a columnar structure. The TiN layer at the right is darker than the AlN at the left as more electrons are scattered by the heavier element, Ti. The t/λ value for the $Ti_xAl_{1-x}N$ layers in Fig. 4(c) of about 0·75 is fairly constant within each layer (except for some small particles which are artefacts of the sputtering process), confirming that the area

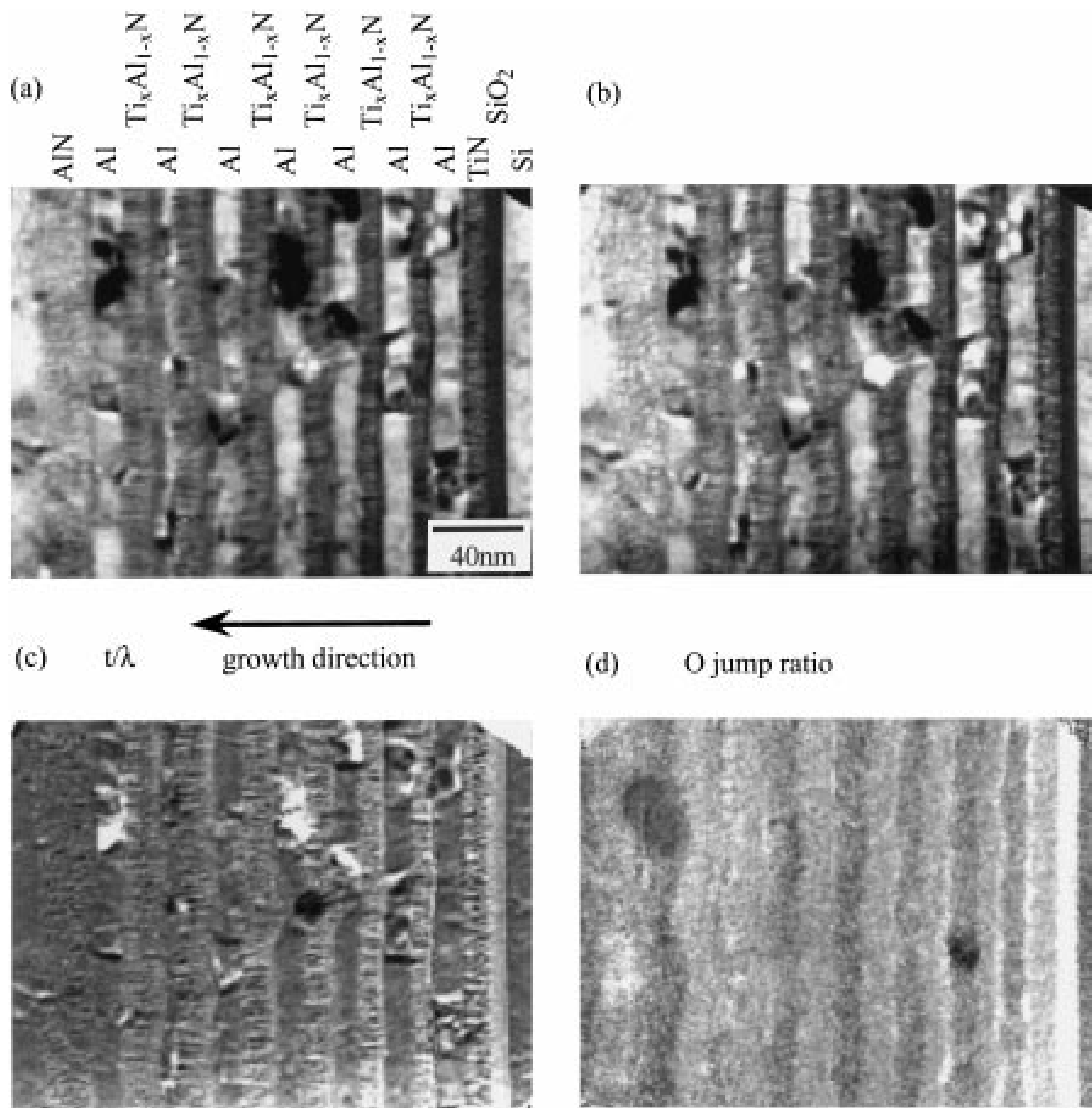

Fig. 4. Bright field images of the $Ti_xAl_{1-x}N$ layers: (a) unfiltered, (b) filtered with the slit centred at 0 eV, (c) t/λ map calculated by the dividing the unfiltered image by the zero-loss image, (d) oxygen jump ratio image for $Ti_xAl_{1-x}N$ multilayers deposited in Si showing the presence of SiO_2 between the Si substrate and the first TiN layer.

of interest has uniform thickness. Since the thickness is reasonably constant, the slight variation in t/λ between layers results mainly from the difference in inelastic mean free path between Al and $Ti_xAl_{1-x}N$. It thus can be regarded as a composition-sensitive map, showing the distribution of all of the elements at once. For example, the uniform layer without columnar structure between the TiN layer and the Si substrate and distinct from either of the adjacent layers is silicon dioxide, as can be seen from the oxygen jump ratio image in Fig. 4(d), implying that the surface was not cleaned completely before sputtering. Because the AlN layer is almost indiscernible from the adjacent Al layers, the difference in the inelastic mean free path between AlN and Al must be small. The atomic fraction, x, for each of the $Ti_xAl_{1-x}N$ layers can in principle be easily calculated since the TiN layer is available to provide a standard and the thickness is identical for all of the layers. However, for the Ti map for this specimen, the N K edge just precedes the Ti L edge by 50 eV, making background estimation using the three-window technique difficult. Given that the two-window technique still cannot account for the background properly, a modified three-window method was used with

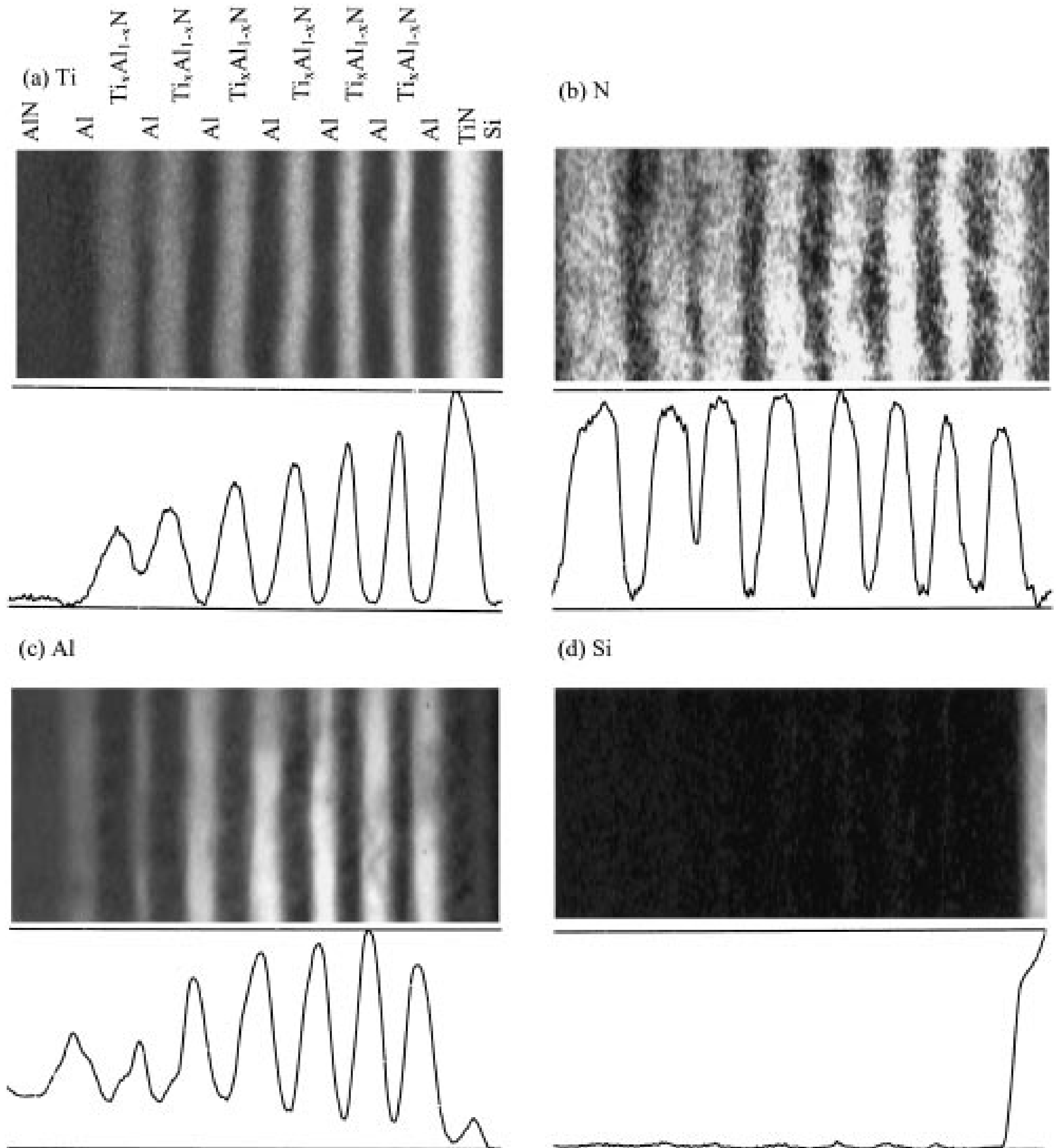

Fig. 5. Elemental maps of (a) Ti, (b) N, (c) Al, (d) Si for $Ti_xAl_{1-x}N$ sample using the ordinary three-window technique where the pre-edges were centred at 360 eV and 380 eV for N, 1470 eV and 1520 eV for Al and 1750 eV and 1800 eV for Si, while the post-edges were centred at 405 eV for N, 1585 eV for Al and 1865 eV for Si.

one pre-edge window at 440 eV, one window on the Ti white lines at 460 eV plus one post-edge window at 480 eV, all with a slit width of 20 eV. The background is estimated to be the average of the pre-edge and the post-edge filtered images since the Ti L edge has sharp white lines and is used to form the elemental map as shown in Fig. 5(a). This method is found to be reasonably good since the intensity of non-Ti containing areas is not far from zero. The N, Al and

Table 1. Atomic fraction of Ti from ESI and EELS for a variety of background subtraction methods, where:
ESI[1] = Ti map obtained without dividing by the 0 eV image and background fitted by linear approximation from the average of images either side of the Ti peak.
ESI[2] = same as above except background fitted by an inverse power law approximation taken also from images either side of the Ti peak.
ESI[3] = Ti map obtained by dividing by the 0 eV image and fitting a background by linear approximation from the average of images either side of Ti peak.
EELS[1] = background fitted using the same method applied to ESI imaging in ESI[1].
EELS[2] = background removed using an inverse power law approximation fitted before the N L edge and a similar background removed from the Ti peak.

Layer sequence	1	2	3	4	5	6
ESI[1]	0·90	0·80	0·66	0·50	0·43	0·29
ESI[2]	0·80	0·70	0·55	0·40	0·33	0·21
ESI[3]	0·80	0·62	0·48	0·31	0·23	0·15
EELS[1]	0·86	0·85	0·66	0·58	0·45	0·29
EELS[2]	0·82	0·80	0·73	0·55	0·35	0·32

Si maps are shown in Figs 5(b)–(d) obtained using the ordinary three-window technique. The maps in Fig. 5 have been divided by the 0 eV loss image to compensate for the diffraction contrast. The Ti map shows clearly that the Ti intensity increases linearly from the left to the right, as shown in the projected intensity profile in Fig. 5(a), while the Al signal is much lower than from the adjacent pure Al layers. Very encouragingly, the N intensity is approximately the same for every layer, implying that diffraction effects have been corrected for and the growth is uniform. The Ti atomic fraction was thus measured for the centre of each layer by comparison with the pure TiN layer for a variety of methods of background estimation including linear and inverse power law background fitting on the map before and after dividing by the 0 eV filtered image and the results are presented in Table 1. In order to investigate the accuracy of these data, a set of EELS spectra was also acquired for all of the layers using a focused probe just covering the width of each layer using a Philips CM30 at 300 kV as shown in Fig. 6. The Ti atomic fraction from this set of EELS spectra was measured in a similar way to that used for the energy filtered images and the Ti atomic fractions are also shown in Table 1. It is apparent that the background calculated from the linear background fit is overestimated, resulting in a higher Ti atomic fraction and vice versa for the inverse power law background fit. The smaller Ti atomic fraction measured from the maps after division by the 0 eV loss image may represent the more accurate fraction. The discrepancy between the results before and after dividing by the 0 eV image might be due to the different plural scattering cross-sections between TiN and $Ti_xAl_{1-x}N$. If our interest here is to estimate the accuracy attainable using ESI, the Ti atomic fraction calculated from EELS spectra and from ESI imaging can be extracted from Table 1 and compared in Fig. 7. The Ti atomic fractions from EELS and those from ESI agree to within 10 at% Ti.

$InAs_xP_{1-x}$ – edges above 1000 eV energy loss

We now turn to a more challenging specimen which is complicated by the fact that the real composition of As in the centre of each delta-doped layer is unknown, the As L edge used for analysis has a high energy loss of 1350 eV and a standard As-containing layer is not available. Because InP damages under the electron beam, each set of images for each element was always taken on a new region of the specimen to minimize knock-on damage. The In map and the In jump ratio image from the specimen (not shown here) revealed that no layer contrast is visible and suggest that In is homogeneously distributed everywhere and that As should substitute for P. This confirms the assumption, that P only replaces the group V atoms, which is always made when quantitative analysis is carried out using other techniques such as HAADF. Nevertheless, the As map also shows no contrast at all (not shown here) for the layers under these experimental parameters for a 20 s exposure time, even though counts of about 1000 per pixel were obtained for each electron spectroscopic image. Figure 8 shows the electron spectroscopic images at losses of (a) 100 eV, (b) 175 eV and (c) the jump ratio image for P. The reason for using only two windows for the P map is that the P L edge at 150 eV is situated where the background is varying too rapidly to be fitted well using three windows. From the P jump ratio image in Fig. 8(c) the As layers appear bright rather than dark as expected, implying that diffraction contrast still dominates the compositional signal even after dividing by the 0 eV filtered image. In addition, the visibility of the thickness fringes in Fig. 8(c) also suggests there is still a significant contribution from elastic diffraction in this relatively low loss region. That the elemental maps for both As (not shown here) and P (in Fig. 8) suffer from insufficient signal-to-noise ratio is obvious.

Accordingly, the experimental parameters need to be optimized to enhance the composition signal at the cost of resolution. The signal-to-noise calculation shown in Fig. 3 suggests that an objective aperture of 9·3 mrad and a slit width of 50 eV would be required for the current density to be around $1-5\times10^{7}\,A\,m^{-2}$ for a LaB_6 filament at the high magnification needed for this specimen under these conditions. The resolution will deteriorate by a factor of about 2 compared to the optimum predicted by Fig. 2 and it will be too poor if either the objective aperture or the slit width are

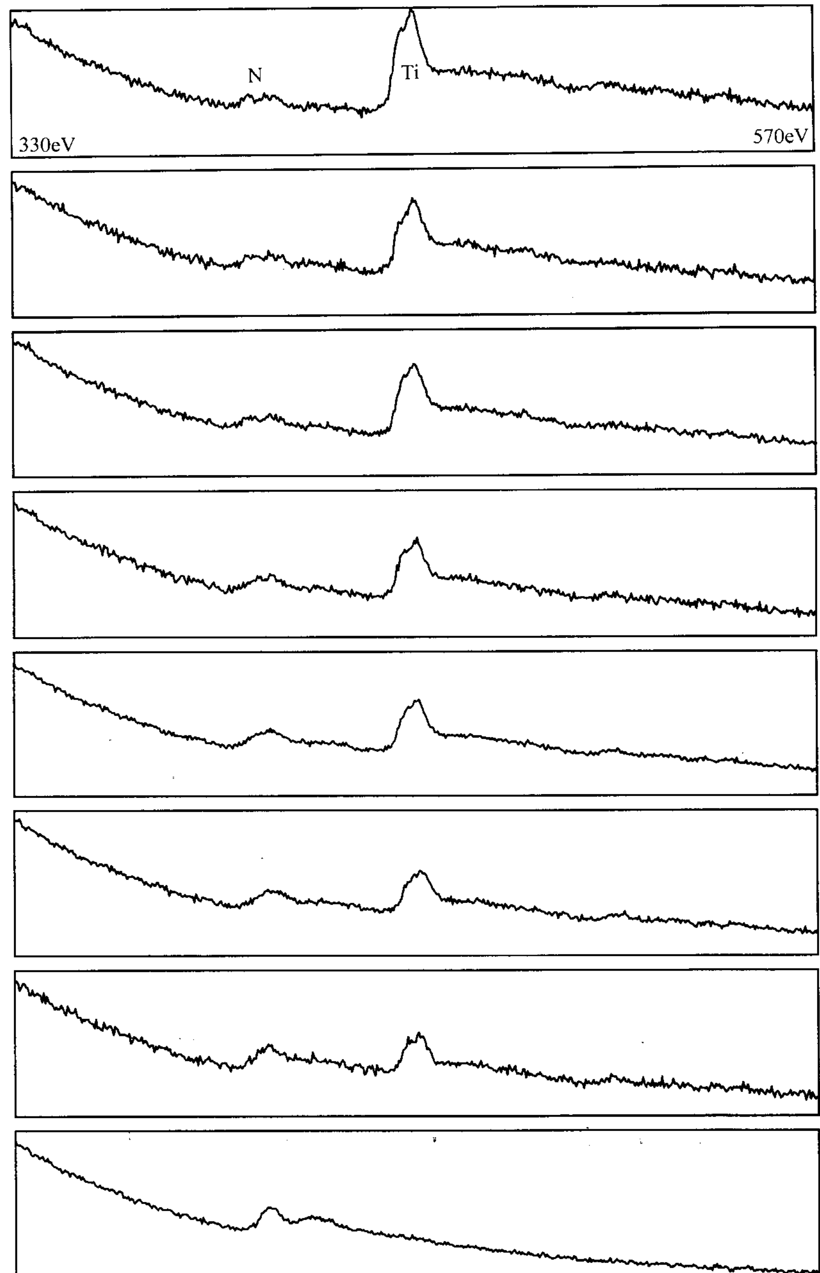

Fig. 6. EELS spectra from each of the $Ti_xAl_{1-x}N$ layers in the $Ti_xAl_{1-x}N$ sample obtained using a focused probe just covering the width of the layer using a Philips CM30 at 300 kV.

further increased. Equally it is unrealistic to use an exposure time longer than 20 s due to both beam damage and specimen drift. By using this new set of experimental parameters, Fig. 8(d) shows the P jump ratio image. The thickness fringes are now absent due to the larger angular range of the inelastically scattered electrons, but unfortunately the layers still appear bright rather than dark, suggesting that the layer contrast is still dominated by diffraction. In fact, the P L edge is very weak, rounded and on a high background (EELS spectra shown in Fig. 9(a)) at this low-loss region resulting in this element being difficult to detect, as Kortje (1996) has also pointed out. Although the P K edge (shown in Fig. 9(b)) is relatively strong compared to the background, its energy loss of around 2240 eV also makes it difficult to detect using a LaB_6 filament. We now consider the suitability of the As L edge at 1350 eV for quantitative analysis of the delta-doped layer composition. Figure 10(a) shows a 0 eV filtered image, showing the regions of the specimen examined while (b) is a t/λ map with intensity contours of 0·5 and 1 marked. The linearity of thickness with distance away from edge of the specimen is demonstrated by the t/λ map, showing that the thickness

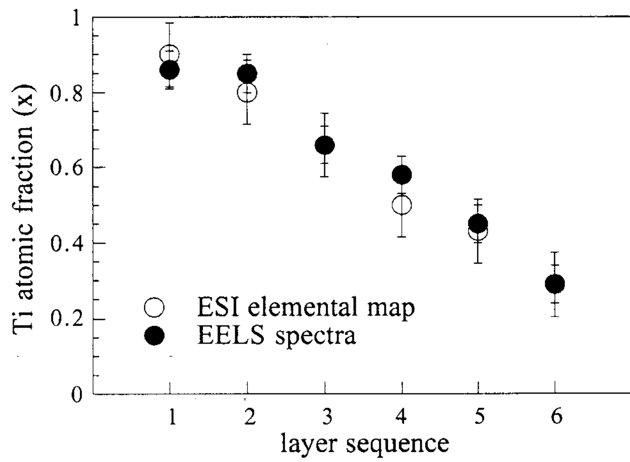

Fig. 7. Ti atomic fraction for each $Ti_xAl_{1-x}N$ layer measured from both the electron spectroscopic images and electron energy loss spectra.

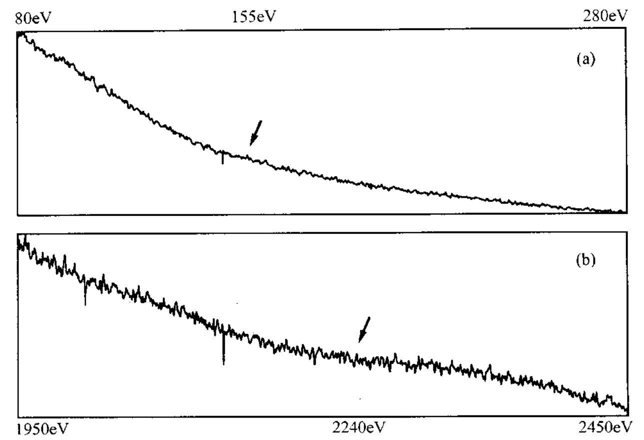

Fig. 9. EELS spectra of InP showing (a) the P L edge which is very weak and round on a high background and (b) the P K edge which is stronger compared to the background but has a much lower count rate.

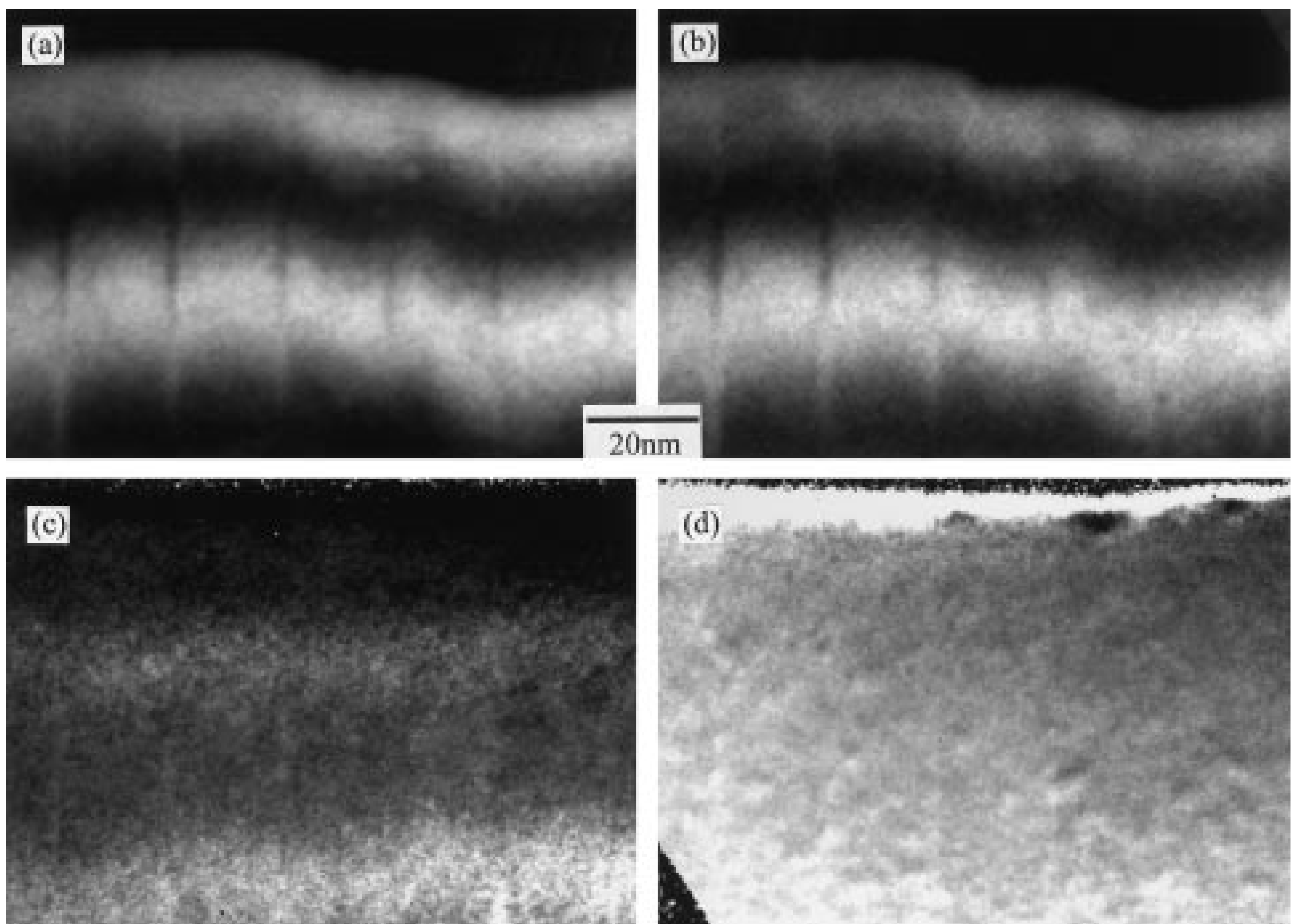

Fig. 8. Energy filtered images at losses of (a) 100 eV and (b) 175 eV corresponding to pre- and post-edge images for P and (c) the jump ratio image for P in $InAs_xP_{1-x}$ using a slit width of 20 eV and an objective aperture of 2·3 mrad. (d) Jump ratio image for P in $InAs_xP_{1-x}$ using a slit width of 50 eV and an objective aperture of 9·3 mrad.

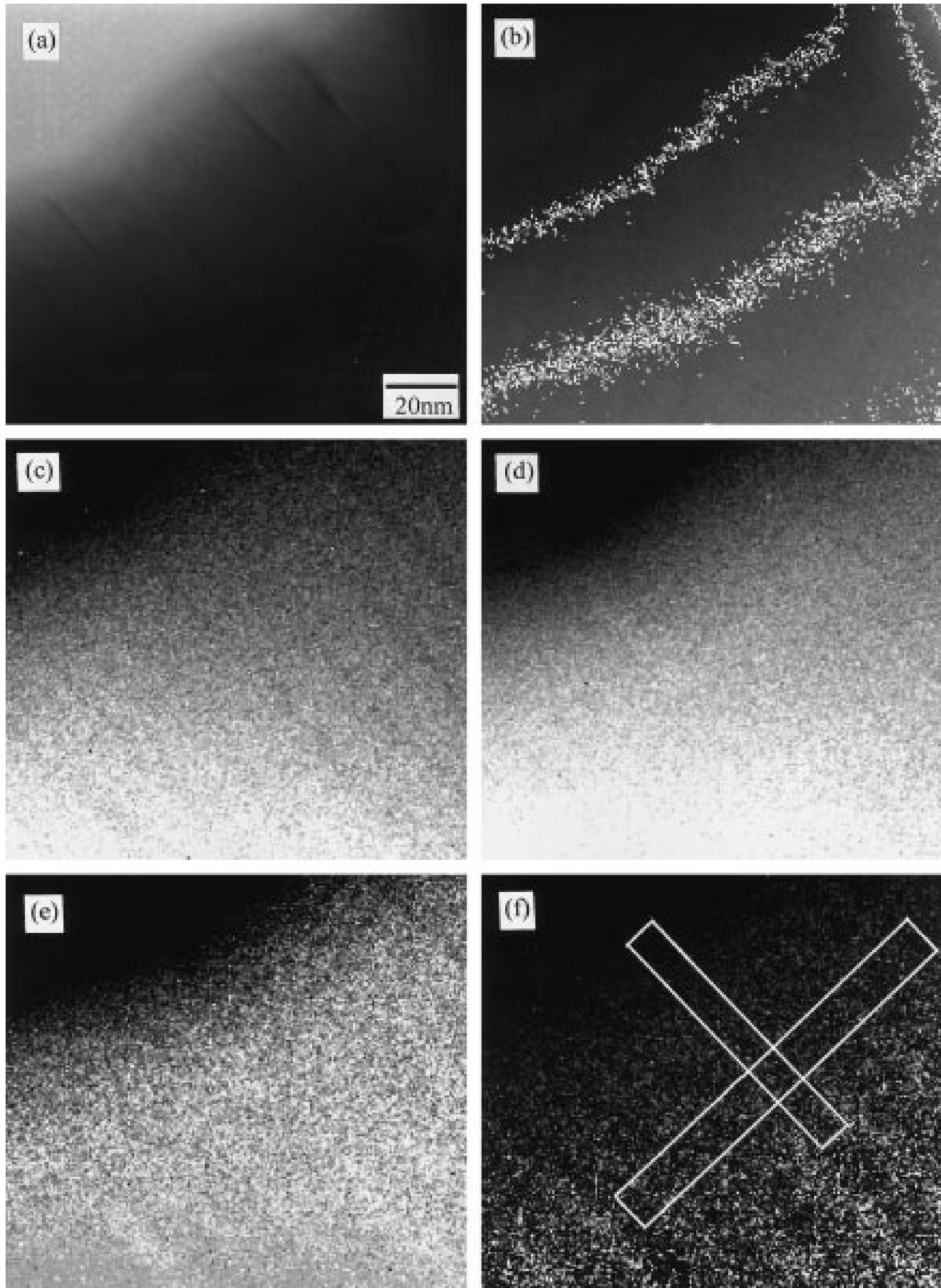

Fig. 10. Electron spectroscopic images around the As edge in $InAs_xP_{1-x}$. (a) A 0 eV filtered image, (b) a t/λ map and images at energy losses of (c) 1280 eV (just before the As edge), (d) 1350 eV (on the As edge), (e) the jump ratio image calculated from (c) and (d), (f) the elemental map calculated from three filtered images.

© 1999 The Royal Microscopical Society, *Journal of Microscopy*, **194**, 58–70

can be measured accurately for quantitative calculations of concentration. Electron spectroscopic images obtained at energy losses of 1280 eV (before the As edge) and 1350 eV (at the As edge) are shown in Fig. 10(c) and (d). The layers in the pre-As edge image are dark but become very faintly bright in the post-As edge image. The As jump ratio image is shown in Fig. 10(e) and the As elemental map is shown in Fig. 10(f) obtained using the three-window method, and both of these images have been divided by the 0 eV filtered image. We can now see that there is enough signal so that the As-containing layers do appear bright in the As map, indicating the presence of As in the delta-doped layers, although the image is noisy and the layers are broadened. No thickness fringes are visible in any of these images, suggesting that diffraction effects can be ignored at these high energy losses and the quantitative concentration of As can now be measured using the integration method (Egerton, 1997) with the calculated partial cross section of $1{\cdot}5 \times 10^{-26}\,\mathrm{m^2\,eV^{-1}}$ for As. However, a suitable range of specimen thickness needs to be chosen for the quantitative calculation. A rectangular region as shown in Fig. 10(f) with its long side perpendicular to the specimen edge was extracted from Fig. 10(f) and then projected to form a one-dimensional profile as a function of thickness, as shown in Fig. 11(a). This profile should be linear if there is little plural scattering. Although Fig. 11(a) is very noisy it can be seen that the As intensity increases until it reaches a maximum, and this is shown more clearly in Fig. 11(b), which is a smoothed version of Fig. 11(a). The change from a linear increase with thickness is at a thickness of around 150 nm corresponding to t/λ of 0·7 in Fig. 10(b), and this compares with t/λ of 1·5 suggested by Egerton *et al.* (1991).

To measure the As concentration in the layers, another rectangular region with a width of 10 pixels covering all of the six layers at the t/λ value of 0·7 (also shown in Fig. 10(f)) was extracted and projected to give a compositional profile as shown in Fig. 11(c) and smoothed in Fig. 11(d), with arrows marking the positions of the layers. It is apparent that the first three layers can be distinguished easily from the background, but not the other three layers. Given that the As concentration has been measured quantitatively previously using the Fresnel contrast and high resolution imaging methods (Liu *et al.*, 1997) to give a total As concentration of around 320 at% (equivalent to 3·2 InAs monolayers if all the As were concentrated together) for the first layer, the minimum detectable As concentration using energy filtered imaging is estimated to be about 80 at% (the deposition time for the third layer is shorter by a factor of 4 than that for the first layer) for this thickness range for quantitative analysis. In order to estimate the error due to the noise, many such profiles have been extracted for thicknesses ranging from 50 to 70 nm and the As concentration for the first layer was measured to be 440 ± 350 at% (where here 440 at% is equivalent to 4·4 InAs monolayers). Of the error, 310 at% is from noise and 40 at% from uncertainty in the thickness measurement. This As concentration can be compared to 315 ± 17 at% obtained from Fresnel contrast (Liu *et al.*, 1997) and 340 ± 20 at% from HAADF (Liu *et al.*, 1999). A comparison of all the techniques which have been applied to this material is shown in Table 2 (please see Liu, 1998, for details). Although the average composition obtained from ESI agrees with the other techniques within experimental error, a fractional error of 80% in the As concentration must be compared to 5% for the other two techniques. Therefore, the quantitative measurement of the As and P elements is limited by the signal-to-noise ratio in ESI. In addition to the total concentration, the average measured layer width of 6·6 ± 1 nm does not represent the true layer width, which is 1·5 nm as measured using the Fresnel method. This broadening by a factor of 4 results

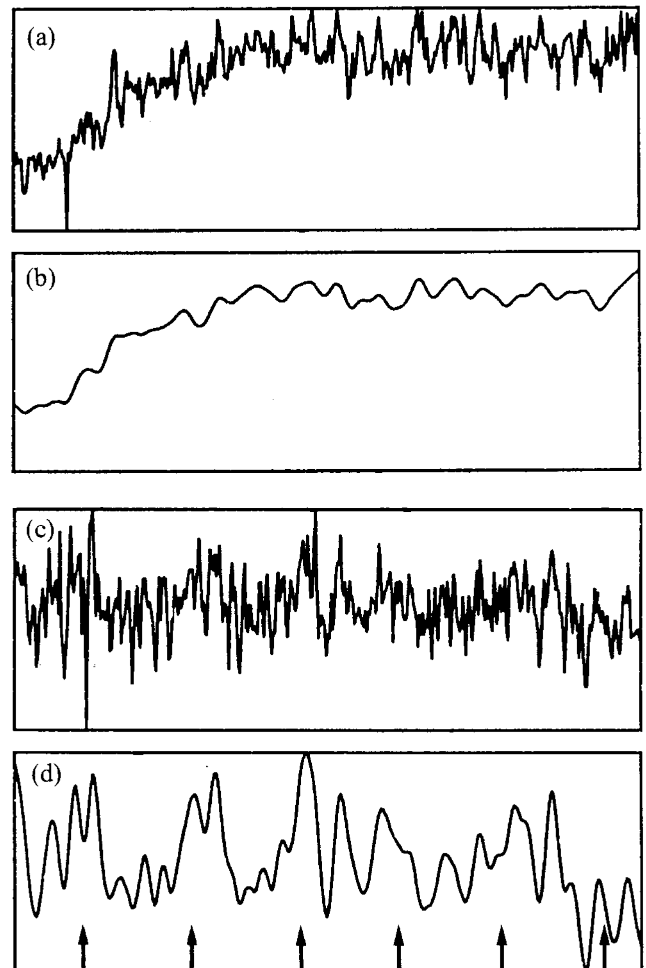

Fig. 11. Intensity profiles projected from the area shown in Fig. 10(f) showing the dependence of the intensity on the (a) specimen thickness with (b) a smoothed version of (a). (c) Projected area across the layers shown in Fig. 10(f) and smoothed in (d).

Table 2. Quantitative data for $InAs_xP_{1-x}$ delta-doped layers in InP characterized by Fresnel contrast, high resolution imaging (HREM), high angle annular dark field (HAADF) and electron spectroscopic imaging (ESI) techniques.

Technique	Fresnel	HREM	HAADF	ESI (this study)
As concentration	315 ± 17 at%	270 ± 40 at%	340 ± 20 at%	440 ± 350 at%
Layer width	1·76 ± 0·3 nm	Not measured	2·1 ± 0·2 nm	6·6 ± 1 nm
Extra information	Dopant profile	Lattice distortion	None	Site occupancy

from specimen drift, instrumental resolution and the signal-to-noise ratio. Given that the instrumental resolution is calculated to be 2 nm and specimen drift is estimated to be 4 nm by comparing the relative layer position in two consecutive electron spectroscopic images, the resolution limited by S/N ratio can be estimated to be about 4 nm.

Discussion and conclusions

For characteristic edges in the low energy loss region for $Ti_xAl_{1-x}N$, the atomic fraction measured from the Ti map after dividing by the 0 eV image is smaller than the atomic fraction without dividing by the 0 eV image. The object of dividing an elemental map by the zero-loss image is to minimize any features due to diffraction effects. However, as the energy loss increases, the diffraction contrast disappears gradually anyway, so that for higher energy losses dividing by the 0 eV loss image increasingly overcompensates for diffraction contrast. In addition, TiN and Al have different plasmon scattering cross-sections, which will be reflected in the intensity of the zero-loss image. Moreover, the plural scattering may redistribute the inelastic electrons since t/λ was rather high at 0·75. However, such effects should be the same for both ESI and EELS, allowing a comparison to be made between these techniques and the accuracy extracted in Section 4 to be still meaningful. The small differences between compositions measured by ESI and EELS can be attributed to the poorer background subtraction possible in ESI, where only two points are available before the edge, and the number of counts per pixel which is much lower.

We have found that specimen preparation by FIB milling or cleaving into 90° wedges helps the quantitative analysis by providing specimens of uniform or uniformly varying thickness. Consequently the quantitative Ti atomic fraction in $Ti_xAl_{1-x}N$ could be measured to an accuracy of ± 10 at%. However, for the As concentration in delta-doped layers of $InAs_xP_{1-x}$, the fractional error was of the order of 80%, caused by the poor signal-to-noise ratio. In this delta-doped specimen, the detection limit of ESI applied to the energy loss region above 1000 eV is estimated to be about 80 at%, while the resolution limit resulting from the low signal-to-noise ratio is about 4 nm.

For the high losses, Al is more visible in $Ti_xAl_{1-x}N$ than As is in $InAs_xP_{1-x}$ despite their edges being at comparable losses, and this is due to the different magnifications involved. At high magnification the incident current density is much lower and the effects of specimen drift are higher, limiting the usable exposure times. We thus find that for measuring the As concentration in $InAs_xP_{1-x}$ the signal-to-noise ratio is the major cause of error.

The formula of signal-to-noise ratio given by Kohl & Berger (1995) shows that there are several ways to improve the signal-to-noise ratio: the use of a high-brightness field emission gun which would allow more electrons to be concentrated on the area of interest at high magnification, increasing the beam convergence, increasing the acquisition time, increasing the width of the energy filter window and using ionization edges with lower energy losses. Since the last four factors have been optimized, it seems that to further improve the spatial resolution and data accuracy a field emission gun is indispensable for elements with characteristic edges above 1000 eV and where high magnifications are needed, such as for semiconductors with ultrathin doping layers.

Acknowledgements

We are grateful to British Telecom and Dr G. S. Chen in Feng-Jia University in Taiwan for the provision of the $InAs_xP_{1-x}$ and $Ti_xAl_{1-x}N$ materials, respectively.

References

Berger, A. & Kohl, H. (1993) Optimum imaging parameters for elemental mapping in an energy filtering transmission electron microscope. *Optik*, **92**, 175–193.

Crozier, P.A. (1995) Quantitative elemental mapping of materials by energy-filtered imaging. *Ultramicroscopy*, **58**, 157–174.

Egerton, R.F. (1997) *Electron Energy-Loss Spectroscopy in the Electron Microscope*, 2nd edn. Plenum Press, New York.

Egerton, R.F. & Crozier, P.A. (1997) The effect of lens aberrations on the spatial resolution of an energy-filtered TEM image. *Micron*, **28**, 117–124.

Egerton, R.F., Yang, Y.-Y. & Chen, F.Y.Y. (1991) EELS of ‘thick’ specimens. *Ultramicroscopy*, **38**, 349–352.

Jager, W. & Mayer, J. (1995) Energy-filtered transmission electron microscopy of Si_mGe_n superlattices and Si–Ge heterostructures I. Experimental results. *Ultramicroscopy,* **59**, 33–45.

Kohl, H. & Berger, A. (1995) The resolution limit for elemental mapping in energy-filtering transmission electron microscopy. *Ultramicroscopy,* **59**, 191–194.

Kortje, K.-H. (1996) ESI contrast analysis: a new approach for element analysis with energy-filtering transmission electron microscopy (EFTEM). *J. Microsc.* **184**, 175–184.

Krivanek, O.L., Kundmann, M.K. & Kimoto, K. (1995) Spatial resolution in EFTEM elemental maps. *J. Microsc.* **180**, 277–287.

Liu, C.P. (1998) *Characterisation of ultrathin semiconductor layers using transmission electron microscopy.* PhD Thesis, University of Cambridge, England.

Liu, C.P., Boothroyd, C.B. & Humphreys, C.J. (1998) Energy-filtered transmission electron microscopy of multilayers in semiconductors. *Electron Microscopy of Semiconducting Materials and ULSI Devices* (ed. by C. Hayzelden, F. M. Ross and C. J. D. Hetherington), pp. 159–164. *MRS Symposium Proceedings*, Vol **523**. MRS, Pittsburgh.

Liu, C.P., Dunin-Borkowski, R.E., Boothroyd, C.B., Brown, P.D. & Humphreys, C.J. (1997) Characterization of ultrathin doping layers in semiconductors. *Microsc. Microanal.* **3**, 352–363.

Liu, C.P., Preston, A.R., Boothroyd, C.B. & Humphreys, C.J. (1999) Quantitative analysis of ultrathin doping layers in semiconductors using high-angle annular dark field images. *J. Microsc.* **194,** 171–182.

Wang, Z.L. (1996) Energy-filtered high-resolution electron microscopy and composition-sensitive imaging. *Microsc. Res. Technique*, **33**, 279–287.